Biophysical Journal Volume 102 April 2012 1617–1626

End-to-End Self-Assembly of RADA 16-I Nanofibrils in Aqueous Solutions

Paolo Arosio,[†] Marta Owczarz,[†] Hua Wu,[†] Alessandro Butté,[‡] and Massimo Morbidelli[†*]

[†]Institute for Chemical and Bioengineering, Department of Chemistry and Applied Biosciences, Zurich, Switzerland; and [‡]Lonza Ltd., LES R&D-DSP Technologies, Visp, Switzerland

ABSTRACT RADARADARADARADA (RADA 16-I) is a synthetic amphiphilic peptide designed to self-assemble in a controlled way into fibrils and higher ordered structures depending on pH. In this work, we use various techniques to investigate the state of the peptide dispersed in water under dilute conditions at different pH and in the presence of trifluoroacetic acid or hydrochloric acid. We have identified stable RADA 16-I fibrils at pH 2.0–4.5, which have a length of ~200–400 nm and diameter of 10 nm. The fibrils have the characteristic antiparallel β-sheet structure of amyloid fibrils, as measured by circular dichroism and Fourier transform infrared spectrometry. During incubation at pH 2.0–4.5, the fibrils elongate very slowly via an end-to-end fibril-fibril aggregation mechanism, without changing their diameter, and the kinetics of such aggregation depends on pH and anion type. At pH 2.0, we also observed a substantial amount of monomers in the system, which do not participate in the fibril elongation and degrade to fragments. The fibril-fibril elongation kinetics has been simulated using the Smoluchowski kinetic model, population balance equations, and the simulation results are in good agreement with the experimental data. It is also found that the aggregation process is not limited by diffusion but rather is an activated process with energy barrier in the order of 20 kcal/mol.

INTRODUCTION

In nanotechnology several functional materials are designed based on the spontaneous self-assembling of single building blocks into highly organized structures (1–3). This bottom-up approach involves a reduction of the total free energy of the system through a combination of weak and strong intra- and intermolecule interactions such as hydrogen forces, ionic bonds, and hydrophobic interactions (4).

Ionic complementary peptides represent a family of monomers able to spontaneously self-assemble in aqueous solutions (5–9). These short, synthetic oligopeptides of 8–16 amino acid residues are either inspired by fragments of naturally occurring proteins or are de novo designed. The peculiar structure of the macromolecules displays on one side completely hydrophobic residues and on the other side positively and negatively charged residues arranged alternatively. Based on charge distributions, one can classify the ionic-complementary peptides into different types: type I: $-+$, type II: $--++$, type III: $---+++$, and type IV: $----++++$ (6). Depending on the intrinsic properties of the structure (e.g., amino acid periodicity, charge distribution, intrinsic chirality, etc.), different peptides have different propensity to form inter- and/or intramolecular hydrogen bonds (6,10), thus leading to different secondary structures (α-helix, β-sheet, or random coil) (11,12) and aggregation states (13). These characteristics make the self-assembly of amphiphilic peptides particularly attractive. For example, one can sensitively tune the charge properties of the peptides, by modifying either their intrinsic structure or the environmental conditions (pH, ionic strength, etc.), to produce in a controlled way various stable and resistant nanomaterials. These include fibrils (4), various types of fibril networks (6), gels (i.e., hydrogels with extremely high water content) (14), and membranes (15). Potential applications have been found for such biocompatible materials in medicine, biotechnology, nanotechnology, and biology. Examples include three-dimensional cell culture (5,16–18), tissue repairing and engineering (15,19,20), cosmetic industry (21), drug release and drug delivery (6,22,23), biological surface engineering (24,25), separation matrices (15), and membrane protein stabilization (3,5). Moreover, self-complementary peptides represent a useful model system to investigate the in vitro formation of amyloid fibrils involved in several neurodegenerative diseases (26).

RADARADARADARADA (RADA 16-I) is a peptide of 16 amino acid residues, belonging to the family of self-complementary peptides. It consists of repeated segments of hydrophobic (alanine) and hydrophilic (arginine and aspartic acid) amino groups (27). RADA 16-I has a high propensity to self-assemble to form very stable β-sheet structures, leading to a series of organized structures. For example, under acidic pH conditions, nanofibrils are observed, whereas higher order nanofibril scaffold are obtained by increasing pH or adding salt (27). RADA 16-I hydrogels with extremely high water content are ideal materials for making three-dimensional scaffolds for cell culture and tissue engineering (16,17). Although significant attention has been given in the literature to the application of RADA 16-I hydrogels, only a few fundamental studies can be found focusing on the aggregation (self-assembling) mechanism (10,27).

Submitted November 9, 2011, and accepted for publication March 2, 2012.

*Correspondence: massimo.morbidelli@chem.ethz.ch

Editor: Heinrich Roder.

0006-3495/12/04/1617/10 $2.00

doi: 10.1016/j.bpj.2012.03.012

The biophysical analysis of RADA 16-I self-assembling mechanism is interesting not only academically but also in practical applications. An example involves the stability of the dispersion of assembled RADA 16-I fibrils, which still limits their industrial productions and handling. Due to the large aggregation propensity, avoiding RADA 16-I assembling into fibrils is extremely difficult. A completely molecular solution of RADA 16-I has in fact never been observed in the literature, and its fibril dispersions represent the starting materials for obtaining scaffolds and gels in practical applications. Moreover, such applications require well-controlled stability of the fibril dispersions to assemble them into desired higher ordered structures.

In this work, we identify the existence of stable fibril units of RADA 16-I at low pH. During their incubation, such fibrils elongate to longer fibrils through end-to-end fibril-fibril association. Several biophysical techniques have been applied to characterize the system. Fibrils size and morphology were characterized by atomic force microscopy (AFM), cryo-scanning electron microscopy (cryo-SEM), transmission electron microscopy (TEM), dynamic light scattering (DLS), and static light scattering. The fraction of RADA 16-I monomers in the system was quantified by size exclusion chromatography (SEC), whereas protein secondary structure was analyzed by circular dichroism (CD) and Fourier transform infrared spectrometry (FTIR). Using such comprehensive characterizations, the stability behavior of the fibril dispersions is investigated as a function of several parameters, such as pH, anion type, and temperature.

MATERIAL AND METHODS

Material

The RADA 16-I (Ac-R-A-D-A-R-A-D-A-R-A-D-A-R-A-D-A-NHCOCH3) peptide was provided by Lonza Ltd. (Visp, Switzerland) as lyophilized powder in the form of chloride and trifluoroacetic salt. The material was used as received without further purification. To prepare the starting material for our investigations, we weighted the peptide powder on a high precision balance (UMT5 Comparator, Mettler Toledo, Greifensee, Switzerland). We then added a suitable amount of buffer solution, followed by mild shaking for 10 min for homogenization. The peptide concentration in the dispersion was measured by ultraviolet (UV) absorbance at 217 nm, and the UV extinction coefficient at 217 nm was estimated equal to 6600 mL/g/cm. For each sample, at least three repetitions were carried out for the concentration measurement. It is worth noticing that for all the experiments shown in this work very similar results have been obtained from three different production batches, with the peptide in the form of both chloride and trifluoroacetic salts.

AFM

10 μL of 150-fold diluted samples were spotted onto a freshly cleaved mica surface for 30 s before washing with Milli-Q deionized water to remove unattached materials and gently drying under nitrogen flux. Samples were imaged at room temperature by a Nanoscope IIIa (Digital Instruments, Tonawanda, NY) operating in tapping mode. A scan rate of 0.8 Hz and antimony-doped silicon cantilevers with resonance frequency in the range 325–382 kHz and tip radius of 8 nm (Veeco, Plainview, NY) were used.

Electron microscopy

Samples for cryo-SEM were vitrified at about -160°C and transferred via the BAL-TEC airlock shuttle system VCT 100 to the freeze-etching unit BAF 060 from BAL-TEC (Balzers, Liechtenstein), where the continuous phase was sublimated under high vacuum at −80°C (within ~120 min) followed by coating with tungsten (2 nm, at 10° angle). Images were recorded on a Gemini 1530 FEG scanning electron microscope (Zeiss, Oberkochen, Germany) equipped with a cold stage.

Samples for TEM were loaded onto a carbon grid (Quantifoil, Jena, Germany) and negative stained with a 2% uranyl acetate aqueous solution. Pictures were recorded on a FEI Morgagni 268.

Light scattering

DLS and static light scattering measurements were performed online using a goniometer, BI-200SM (Brookhaven Instruments, Holtsville, NY) covering angles from $\theta = 16°$ to 150°. A solid-state laser, Ventus LP532 (Laser Quantum, Manchester, UK) with a wavelength $\lambda_0 = 532$ nm was used as the light source.

DLS was also measured at a fixed angle of $\theta = 173°$ using a Zetasizer Nano (Malvern, Worcestershire, UK) with a laser beam wavelength of $\lambda_0 = 633$ nm. Micro UV-cuvettes with dimension 12.5 × 12.5 × 45 mm (70 μL) and light path 1 cm (Brand GmbH, Wertheim, DE) were used.

DLS measures the intensity fluctuation due to the Brownian motion of the particles as a function of the delay time, τ, from which the intensity autocorrelation function $g^2(\tau)$ and the field autocorrelation function $g^1(\tau)$ can be defined

$$g^2(\tau) = \frac{\langle I(q,0)I(q,\tau)\rangle}{\langle I(q)\rangle^2}, \quad (1)$$

$$g^2(\tau) = 1 + \sigma\big(g^1(\tau)\big)^2, \quad (2)$$

where σ is a constant close to 1, depending on the specific configuration of the detector, and q is the scattering wavevector, $q = (4\pi n/\lambda_0)\sin(\theta/2)$, with θ the scattering angle, n the refractive index of the solvent, and λ_0 the wavelength of the laser beam. The field autocorrelation function decays exponentially with τ (28):

$$g^1(\tau) = \exp(-\Gamma\tau), \quad (3)$$

where the decay rate coefficient, Γ, is a function of the particle diffusivity.

SEC

SEC was performed with a Superdex Peptide 10/300 GL, 10 mm × 300 mm size-exclusion column (GE Healthcare, Uppsala, Sweden) mounted on an Agilent 1100 series HPLC unit (Santa Clara, CA) consisting of a quaternary pump with degasser, an autosampler, a column oven, and a DAD detector. Each sample was eluted for 70 min at a constant flow rate of 0.4 mL/min using as mobile phase the same buffer of the analyzed sample. The UV absorbance peaks were detected at 217 nm.

CD

CD spectra were collected using a Jasco-815 CD spectrophotometer (Jasco, Easton, MD). Far-UV CD spectra were recorded from 260 to 190 nm with

the temperature of the cell holder controlled at 25°C. A quartz cuvette with 0.1 cm path length was used. Spectra obtained after buffer subtraction was corrected for protein concentration and smoothed using the Savitsky-Golay function.

FTIR

Hydrated thin film attenuated total reflectance (ATR-FTIR) measurements were performed on a Nicolet Nexus 870 FTIR ESP instrument equipped with an ATR Nicolet Omni-Sampler device (Nicolet, Madison, WI). Aliquots of 10 μL were spotted on the crystal surface and left to dry under nitrogen flux. The spectra were collected in the wavelength range from 1700 to 1600 cm^{-1} at 1 cm^{-1} resolution and smoothed using the Savitsky-Golay function after buffer subtraction.

RESULTS AND DISCUSSION

Characterization of fibril size and morphology

After the peptide powder is dissolved in water at a concentration in the range of 0.5–1 g/L, a transparent homogeneous solution is obtained (see Fig. S1 in the Supporting Material). The AFM analysis in Fig. 1 *a* shows the presence of a significant amount of nanoscale fibrils with length in the range of ~200–400 nm, which is consistent with previous findings in the literature (27). Notably, the obtained fibrils cannot be further broken by either sonication or shaking or stirring, indicating that these short fibrils exhibit high resistance against shearing forces.

Three different solvents were used to dissolve the peptide: Milli-Q deionized water (pH was automatically shifted to around 4.5 due to the counterions of the lyophilized peptide), 0.013 M trifluoroacetic acid (TFA) solution at pH 2.0 and 0.01M hydrochloric acid (HCl) solution at pH 2.0. In each solution, the fibril length distribution was evaluated from the AFM pictures by manually counting and measuring the length of the fibrils. Under each condition at least three independent samples and 350 fibrils were considered to ensure statistical reliability. Fig. 1 *b* shows the fibril length distributions in the three solutions at the peptide concentration of 1 g/L. All the distributions are rather similar in shape but the average length is slightly dependent on pH. The mean length and the standard deviation of the fibril distributions are respectively 296 and $\pm$131 nm in water at pH 4.5, 370, and $\pm$134 nm in TFA solution at pH 2.0, 332, and $\pm$138 nm in HCl solutions at pH 2.0.

To obtain more details on the fibril structure, we have analyzed the samples using both cryo-SEM and TEM. As shown in Fig. 1, *c* and *d*, both techniques confirm the length distribution obtained from AFM. The fibril diameter in all the considered solutions is ~14 nm according to AFM and cryo-SEM pictures and ~10 nm according to TEM pictures. It is well known that due to the excluded volume of the AFM tip during the tipping of the surface, the fibril diameter measured by AFM cannot be considered reliable. Moreover, the drying procedure necessary during sample preparation for AFM and cryo-SEM analysis could induce flattening of the fibril structure on the surface. Because TEM requires very mild drying conditions, the fibril diameter given by TEM can be considered the most reliable. However, also in this case the staining technique could affect the results. Therefore, a detailed model of the peptide fibrils cannot be obtained with any of the applied techniques.

It is known that the length and the height of a RADA 16-I peptide in a stretched conformation are equal to 5 and

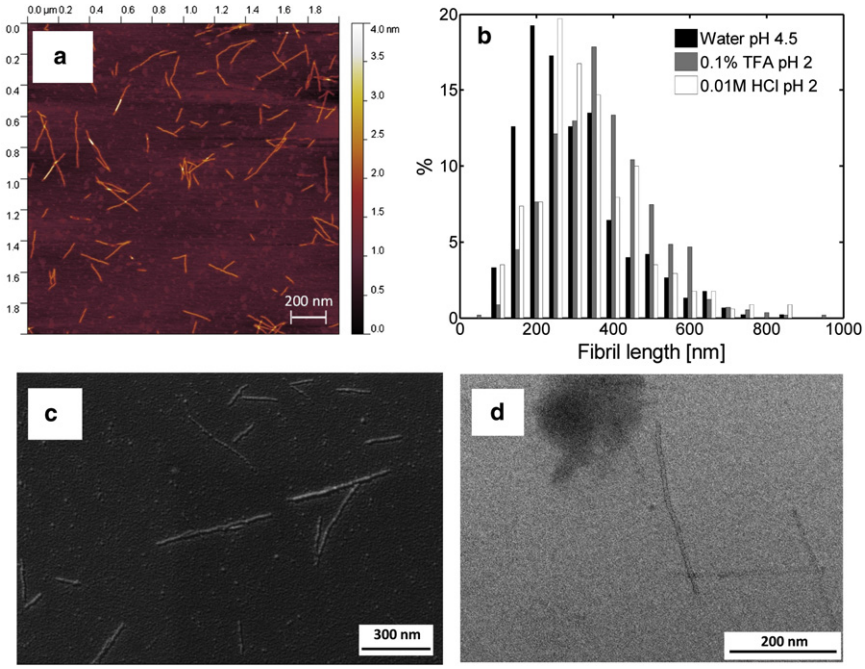

FIGURE 1 (*a*) Typical AFM picture showing the presence of nanofibrils in the dispersions. (*b*) Fibril length distribution obtained from AFM pictures, in the freshly prepared peptide dispersion in several aqueous solutions. (*c* and *d*) Cryo-SEM (*c*) and TEM (*d*) pictures of the fibrils in the aqueous dispersions of the RADA 16-I lyophilized powder at pH 4.5 and concentration of 0.5 g/L.

1.3 nm, respectively (27). On the basis of the mechanism proposed in the literature (6,13), the peptides form the fibrils by aggregation along their stretched backbone via hydrogen bonding. In this way, the obtained fibrils would have a width or diameter of ~5 nm, which is only half of the value determined from TEM in Fig. 1 *d*. On the other hand, the fibrils could also further assemble by lateral association into thicker fibrils (13). The observed width or diameter of 10 nm would then indicate that the observed fibril is composed of two fibrils joined together by lateral association. No twisting of the fibrils occurs, according to the TEM picture in Fig. 1 *d*. The height of the fibrils has been evaluated from the AFM pictures equal to 1.16 ± 0.22 nm, rather consistent with the height of the RADA-I peptide.

In parallel with microscopy analysis, the fibrils size was analyzed by light scattering (LS) techniques. For an asymmetric particle, the decay rate coefficient, Γ, of the field autocorrelation function in dynamic LS is composed of two terms: one related to the translational diffusion (D) and another to the rotational motion of the particle along its axis (Θ) (29):

$$\Gamma = D \cdot q^2 + \Theta. \tag{4}$$

The decay rate coefficient Γ has been evaluated with two different instruments at different angles and plotted in Fig. 2 *a* as a function of q^2. This shows that all the data can be well represented by a straight line with a negligible intercept (i.e., Θ~0), indicating that for the given fibril system, the contribution of the rotational diffusion is negligible. The estimated translational diffusion coefficient is $D = 6.6\ \mu m^2/s$.

Let us assume that the short RADA 16-I fibrils are rigid and rod-like. The fibril dimension can then be estimated from the translational diffusion coefficient according to the Doi-Edward relationship (30):

$$D = \frac{kT}{3\pi\eta L} \ln\left(\frac{L}{b}\right), \tag{5}$$

where k is the Boltzmann constant, T the temperature, η the solvent viscosity, L and b the length and the diameter of the fibril, respectively. For a polydisperse system, the measured diffusion coefficient is a z-average value, $\langle D \rangle_z$, which can be computed from the length distribution of individual fibrils (31):

$$\langle D \rangle_z(q) = \frac{\sum_{i=1}^{N} N_i \cdot D_i \cdot P_i(q) \cdot L_i^2}{\sum_{i=1}^{N} N_i \cdot P_i(q) \cdot L_i^2}, \tag{6}$$

where N_i is the number concentration of fibrils with length L_i and $P_i(q)$ is the form factor for a rigid rod with length L_i at the wavevector q, given by (32):

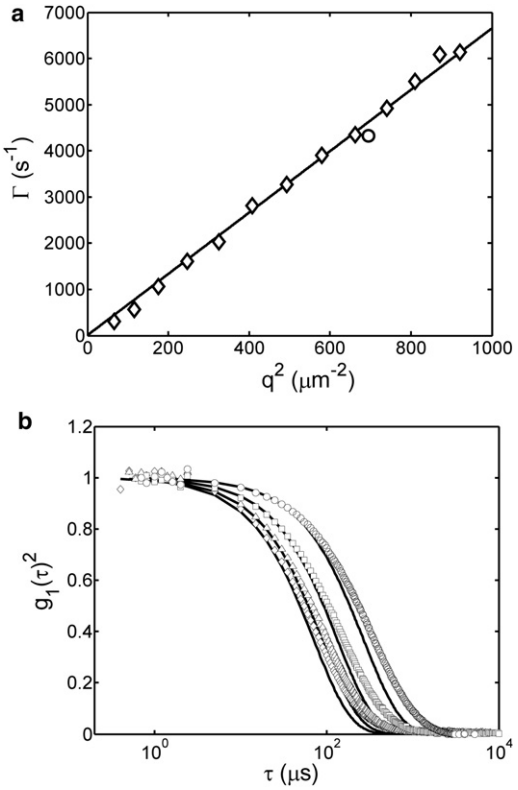

FIGURE 2 (*a*) Decay coefficient of the DLS measurements, Γ, as a function of the wavevector, q^2, measured using BI-200SM (Brookhaven) (◇) and Nanosizer (Malvern) (○). The continuous line is the best fit of $\Gamma = D \cdot q^2$ with $D = 6.6\ \mu m^2/s$. (*b*) Measured autocorrelation functions at the angles, 60° (○), 90° (□), 120° (Δ), and 150° (◇), compared with the computed ones using Eq. 3 (*continuous line*).

$$P_i(q) = \frac{2}{qL_i} \int_0^{qL_i} \frac{\sin(x)}{x} dx - \left[\frac{2}{qL_i} \sin\left(\frac{qL_i}{2}\right)\right]^2. \tag{7}$$

From the fibril length distributions determined from AFM in Fig. 1 *b* and the D_i values of individual fibrils computed from Eq. 5 considering $b = 10$ nm, we have calculated the $\langle D \rangle_z$ value from Eq. 6. The obtained $\langle D \rangle_z$ values are only slightly dependent on the scattering angle: 7.9 $\mu m^2/s$ at 173° and 7.7 $\mu m^2/s$ at 60°, and are reasonably in agreement with the value (6.6 $\mu m^2/s$) from the DLS measurement. As a consequence, from the calculated $\langle D \rangle_z$ values we can predict the autocorrelation function at different angles, and the obtained results are compared to the measured ones in Fig. 2 *b*. As can be seen, the agreement is rather satisfactory. The difference at large delay times occurs because we have used a single Γ value in the autocorrelation function simulations, without accounting for the polidispersity of the samples.

Given the low peptide concentration (0.5–1 g/L), we can consider the fibril dispersions as dilute systems. The form factor of the fibrils, $P(q)$, can then be determined from the

static LS experiments, i.e., from the measured intensity at different angles, $I(q)$ (33):

$$P(q) = \frac{I(q)}{I(0)}, \tag{8}$$

where $I(0)$ is the intensity at zero angle.

For an ensemble of polydisperse rods, the average form factor, $\langle P(q)\rangle$, can then be expressed using Eq. 7 as follows (34):

$$\langle P(q)\rangle = \frac{\sum_{i=1}^{N} N_i \cdot P_i(q) \cdot L_i^2}{\sum_{i=1}^{N} N_i \cdot L_i^2}. \tag{9}$$

Using the fibril length distribution in Fig. 1 *b*, we have computed the average form factor, $\langle P(q)\rangle$, from Eqs. 7 and 9, and the result is compared with the measured $\langle P(q)\rangle$ in Fig. 3. It can be seen that the calculated $\langle P(q)\rangle$ represents well the experimental data.

The radius of gyration of a rigid rod can be calculated from its length, as $R_g^2 = L^2/12$ (33). Thus, the average radius of gyration of our fibrils, $\langle R_g\rangle$, can also be computed from the known fibril length distribution in Fig. 1 *b*, using the following expression (35):

$$\langle R_g\rangle^2 = \frac{\sum_{i=1}^{N} N_i \cdot R_{g,i}^2 \cdot L_i^2}{\sum_{i=1}^{N} N_i \cdot L_i^2}. \tag{10}$$

The obtained value is $\langle R_g\rangle = 125$ nm, which is in good agreement with that estimated from the form factor based on the Guinier plot (114 nm). Therefore, the in situ LS measurements correlate well with microscopy characterizations and also confirm the reliability of the measured fibril length distributions in Fig. 1 *b*.

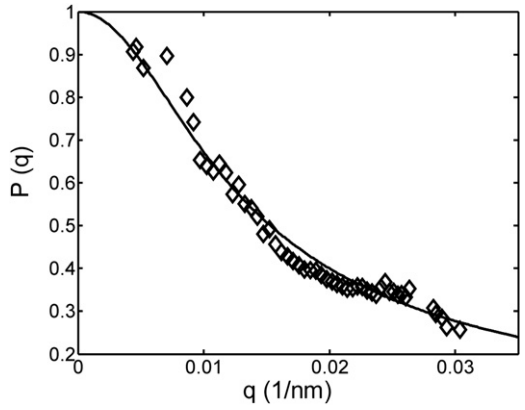

FIGURE 3 Average form factor, $\langle P(q)\rangle$ of the fibrils, measured by static light scattering (*symbols*), compared with the calculated one (*solid curve*) according to Eq. 9.

It is difficult to determine whether or not the monomeric form of the peptide is present in the system using LS techniques, because of the substantial difference in size between the monomers and the fibrils. The size of the monomers is also below the lower limit of the used microscopy techniques. Thus, we have applied SEC to quantify the monomers. Different cutoff (20 nm and 220 nm) filters were applied to prepare the samples to verify that no artifacts were induced by the filtering procedure. It is found that in the aqueous solution at pH 4.5 no monomer can be detected, whereas at pH 2.0, apart from the fibrils, we have observed 60 ± 25% monomers both in the TFA as well as in the HCl solution. It is worth noticing that the amount of monomers determined by SEC at low pH varies significantly even though the same preparative procedure was rigorously followed for several repetitions. This is likely due to the difference in the fibril length distributions of different resuspensions of the same powder even at the same concentration. In fact, the distributions reported in Fig. 1 *b* are the average of different resuspensions. At a given peptide concentration, samples with a shorter average size contain more fibrils than those with a larger average size, thus possessing more fibril ends from which the monomers can detach. An undetectable amount of monomers at pH 4.5 in the aqueous solution was confirmed by several repetitions.

From the previous results, we can then conclude that all the peptides in the original powder are practically in the form of fibrils, and the presence of monomers at low pH is likely due to the dissolution of the fibrils. It is in fact well known that TFA is able to dissolve protein aggregates into monomers by disrupting the hydrogen bonds (36). From our present results, we see that HCl can also be used for the same purpose.

To better understand the state of the peptides under different conditions, we have investigated their secondary structure both in the solution and in the original powder, using FTIR and CD. Due to the well-known interference between TFA and protein in the I-amide region, the peptide dispersion in the TFA solution was not analyzed by FTIR. In Fig. 4 *a* the FTIR spectra of the peptide in water at pH 4.5 and in the original powder are shown. They are rather similar and show a maximum at 1627 cm^{-1}, characteristic of the β-sheet structure. A significant shoulder in the range of 1650–1670 cm^{-1} indicates the presence of β-sheet turn structures, as observed in other amphiphilic peptide systems (37). These results suggest that the peptides in water at pH 4.5, as well as in the original powder, possess an ordered structure, i.e., fibrils, thus confirming that the monomers at pH 2.0 come from dissolution of the fibrils.

Fig. 4 *b* shows the CD spectra of the peptide dispersion in water at pH 4.5 and in the 0.013 M TFA solution at pH 2.0. For the former, the minimum at 215 nm clearly indicates the β-sheet structure, thus consistent with the FTIR data. For the latter, instead, the minimum is located at 200 nm, characteristic of random coil, more disordered structures. Since in

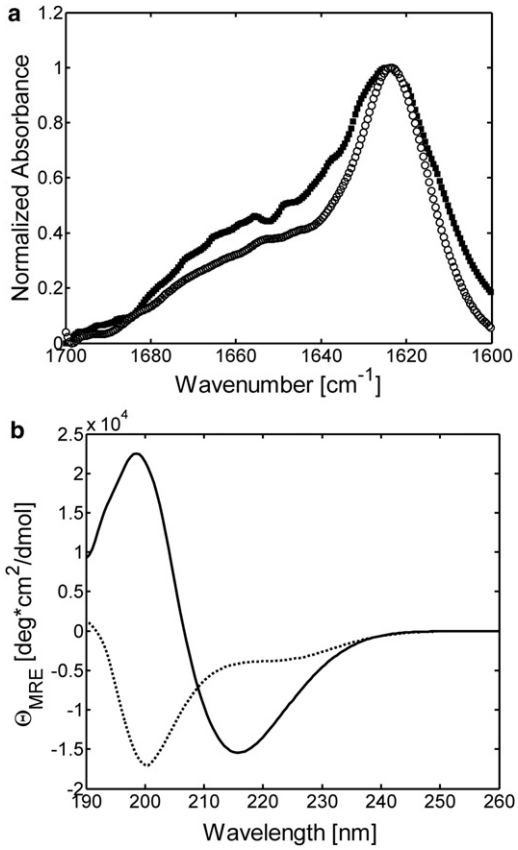

FIGURE 4 (*a*) FTIR spectra of the lyophilized RADA 16-I powder (■) and its dispersion in water at pH 4.5 (○), and (*b*) CD spectra of the RADA 16-I dispersion in the 0.013 M TFA solution at pH 2.0 (*dashed curve*) and in water at pH 4.5 (*solid curve*).

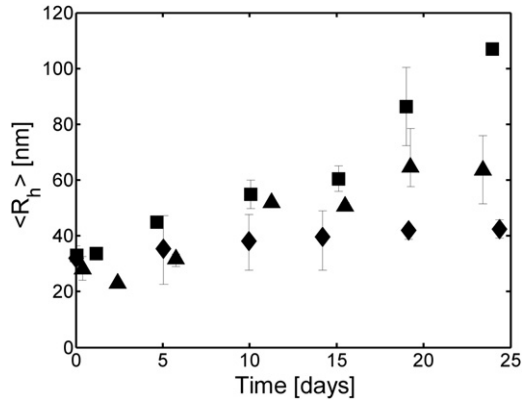

FIGURE 5 Time evolution of the average hydrodynamic radius, $\langle R_h \rangle$, of the fibrils in the 0.013 M TFA solution at pH 2.0 (■), in the 0.01 M HCl solution at pH 2.0 (▲), and in distilled water at pH 4.5 (◆), measured at 25°C and peptide concentration of 1 g/L.

this case the monomers are present, this result indicates that the monomers exhibit a random coil structure in the aqueous solution. The shoulder around 215 nm corresponds to the remaining fibrils. According to CDpro analysis (see Table S1), the amount of β-strand is 65.5% at pH 4.5 and 13.2% at pH 2.0, whereas the unordered structure content is 10% at pH 4.5 and 66.1% at pH 2.0.

Stability and aggregation kinetics

We have monitored the stability of the fibril dispersions at room temperature in three aqueous solutions: water at pH 4.5, 0.013 M TFA solution at pH 2.0, and 0.01 M HCl solution at pH 2.0, respectively, at the peptide concentration of 1 g/L, using DLS. In Fig. 5 the measured average hydrodynamic (or equivalent-sphere) radii, $\langle R_h \rangle$, are shown as a function of the incubation time. In all three solutions, the $\langle R_h \rangle$ value of the fibrils increases with time slowly, indicating the occurrence of slow aggregation of the fibrils. The aggregation rate in the three solutions follows the order, 0.013 M TFA at pH 2.0 > 0.01 M HCl at pH 2.0 > water at pH 4.5. Because the isoelectric point of RADA 16-I is pI = 7.2 (10), at both pH 4.5 and 2.0 the net charge on the surface is positive. The net charges of RADA16-I monomer calculated from the pK values of the amino acid side chains (38) are about +0.75 at pH 4.5 and +4 at pH 2.0, and, in fact, the zeta potential values are 36.2 mV in water at pH 4.5 and 40.8 mV in 0.013 M TFA at pH 2.0 (details of zeta potential measurements are reported in the Supporting Material). Therefore, the better stability of the fibril dispersion in water at pH 4.5 cannot be explained by the charging effect. We believe that it results from the hydrophobic effect. In particular, at pH 2.0 more aspartic residues are protonated, leading to an increase in the hydrophobicity of the peptide, thus in the propensity to aggregation in water. TFA is a strong counterion-pairing agent (39) and has a larger propensity to bind charged groups with respect to Cl (see Fig. S2). The larger aggregation extent in the 0.013 M TFA solution than in the 0.01 M HCl solution at pH 2.0 is consistent with the more efficient reduction of the surface charges, thus promoting the aggregation, in this case due to a charging effect.

For the fibril dispersion in water at pH 4.5, because negligible monomers are present, the observed aggregation is clearly due to fibril-fibril aggregation. In the 0.013 M TFA and 0.01 M HCl solutions at pH 2.0, however, the characterization results shown in the previous section indicate that the system contains a substantial amount of monomers. It would then be reasonable to consider the participation of the monomers in the aggregation, particularly considering that they would be favored with respect to fibril-fibril aggregation due to their higher diffusivity. However, after a detailed SEC analysis of samples taken along the incubation time, we found that although the amount of the monomers decreases with time, several peaks at longer eluting times, representing molecules smaller than RADA 16-I, appear and increase with the incubation time, as clearly shown in Fig. 6 *a*. Mass spectrometry analysis confirmed the

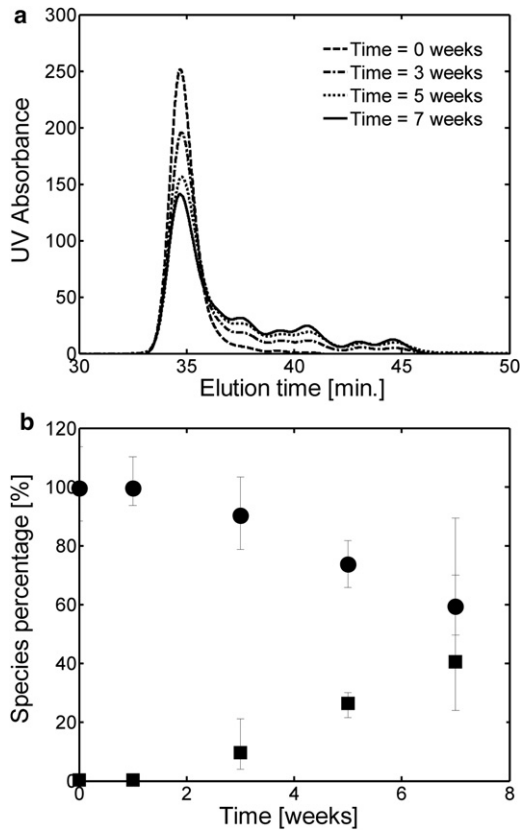

FIGURE 6 For the peptide distribution in the 0.01 M HCl solution at pH 2.0: (*a*) SEC chromatograms at several incubation times, where the peak at the eluting time of 34 min represents the monomer, RADA 16-I, and (*b*) percentage of the SEC chromatogram area corresponding to the remaining monomers (●) and the fragments eluting at larger times (■).

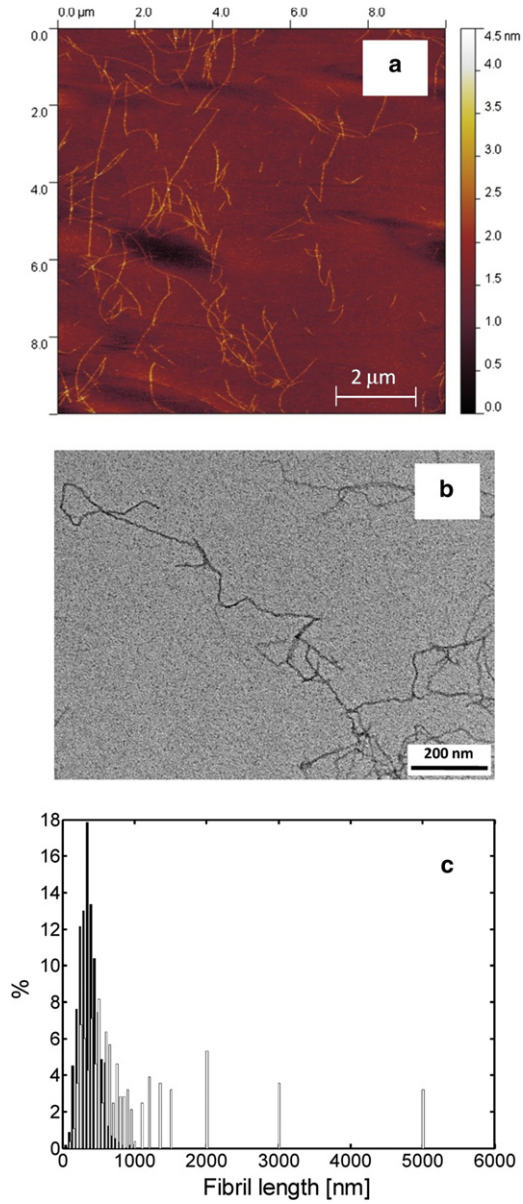

FIGURE 7 AFM (*a*) and TEM (*b*) pictures of the fibrils in the RADA 16-I dispersion in the 0.013 M TFA solution at pH 2.0 and at the peptide concentration of 1 g/L after 25 days incubation, and (*c*) fibril length distributions obtained from the AFM pictures at time 0 (*black*) and after 25 days incubation (*white*).

fragmentation of the monomeric RADA16-I into smaller molecules (Fig. S3). More importantly, as shown in Fig. 6 *b*, the area of the SEC chromatogram for the RADA 16-I peak decreases and the total area for the smaller molecules peaks increase as the incubation time increases, whereas the area sum of all the peaks remains practically constant. These results indicate that the decrease in the amount of monomers along the incubation time is not due to aggregation to fibrils. It is instead related to some chemical degradation of the peptides (e.g., hydrolization) at low pH. On the other hand, this result reveals that, similar to the case at pH 4.5, the increase in the fibril size is also due to fibril-fibril aggregation.

Samples at the incubation time of 25 days have been analyzed by AFM and TEM, and the corresponding pictures are shown in Fig. 7, *a* and *b*, respectively. The most important observations from these pictures, as well as from the fibril length distributions shown in Fig. 7 *c*, are that the fibrils become longer but their diameter remains the same as before the incubation. The same result has been found for fibrils incubated in water at pH 4.5 for 5 months (Fig. S4). This suggests that the main mechanism responsible for the fibril aggregation is the end-to-end fibril elongation, and that lateral aggregation is negligible. Such mechanism is consistent with the sliding diffusion dynamic reassembly proposed by Yokoi and co-workers for the RADA 16-I fibril aggregation (27). They showed that after sonication and breakage of longer fibrils, the fragmented fibrils reassemble into the original fibrils, due to the unpaired hydrophobic and hydrophilic patches at the end of the fibril created by the breakage.

The previous results have been confirmed by incubation at higher temperatures to accelerate the aggregation. As

can be seen from Fig. 8, increasing temperature induces both faster aggregation kinetics and faster peptide degradation.

Let us now apply the Smoluchowski kinetic approach, i.e., the population balance equations (PBE), to simulate the growth of the fibrils, based on the end-to-end fibril-fibril aggregation mechanism. The PBE in this case can be written as

$$\frac{dN_i}{dt} = \frac{1}{2}\sum_{j=1}^{i-1} k_{j,i-j}N_jN_{i-j} - N_i\sum_{j=1}^{\infty} k_{ij}N_j, \qquad (11)$$

where N_i is the number concentration of fibrils with length i, and k_{ij} the rate constant for the aggregation between two fibrils with length i and j, respectively. The first and the second terms on the right side of Eq. 11 represent the birth and death of the fibril of a given length, respectively. The aggregation rate constant can be expressed as

$$k_{ij} = \alpha \cdot k_{ij}^{Diff}, \qquad (12)$$

where k_{ij}^{Diff} is the rate constant for diffusion-limited aggregation and α ($\in[0,1]$) is a parameter representing the efficiency of the aggregation with respect to the diffusion-limited aggregation. Following Hill (40) and Pallitto and Murphy (41), k_{ij}^{Diff} for the end-to-end fibril aggregation can be expressed as

$$k_{ij}^{Diff} = \frac{k_BT}{3\eta}\frac{N_A}{1000}\frac{(\delta\cdot\omega)^2}{L_i+L_j}\left(\frac{\ln(L_i/b)+\nu_i}{L_i}+\frac{\ln(L_j/b)+\nu_j}{L_j}\right),$$
$$\nu_i = 0.312 + 0.565(L_i/b)^{-1} - 0.100(L_i/b)^{-2}, \qquad (13)$$

where T is temperature, k_B the Boltzmann constant, N_A the Avogadro number, η the viscosity of the solvent, ω the minimum allowed angle between two fibrils, and δ the minimum allowed distance between two fibrils. A reference value from the literature was used for $\delta\cdot\omega$ ($= 4.5 \times 10^{-10}$ cm rad) (42), and it was assumed temperature independent. The parameter α in Eq. 12 was used as an adjustable parameter to reproduce the experimental fibril length distributions (see the Supporting Material for details).

By numerical integration of the PBE, we obtain the time evolution of the fibril distribution, from which the corresponding average hydrodynamic radius, $\langle R_h\rangle$, can be evaluated from the average diffusion coefficient, $\langle D\rangle_z$, calculated according to Eq. 6. The fibril distribution estimated from the AFM pictures in Fig. 1 *b* has been considered as the initial condition. The simulated curves are compared with the experimental data at different aggregation temperatures in Fig. 8 *a*. It can be seen that the model simulation results are in good agreement with the experimental data when the fibrils are small. As the fibril length increases, due to the fibril flexibility, bending, curvature, etc., the fibrils cannot be modeled as rod-like objects. As a consequence, the expressions of the R_h and of the aggregation rate considered in the model do not apply anymore, and the simulation results deviate significantly from the experimental data. The α-values obtained from the simulations at different conditions are summarized in Table 1: all of them are substantially smaller than unity, indicating that all the investigated aggregation processes are substantially slower than diffusion-limited aggregation. Thus, the aggregation rate is not controlled by diffusion but rather an activated process that requires the overcoming of some activation energy barrier. This is estimated to be in the order of 20 kcal/mol by considering the Arrhenius-type behavior of k_{11} (Eq. 12): $k_{11} = k_0\exp(-E_{Att}/RT)$, as shown in Fig. S6.

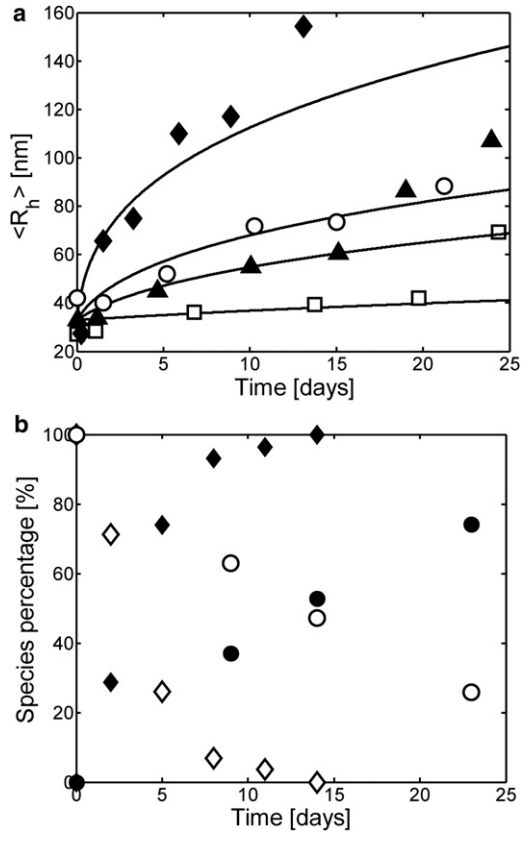

FIGURE 8 (*a*) Measured time evolutions of the average hydrodynamic radius, $\langle R_h\rangle$, of the fibrils in the 0.013 M TFA solution at pH 2.0 at $T =$ 4°C (□), 25°C (▲), 37°C (○), and 50°C (◆), compared with the PBE simulations (*solid curves*) based on Eq. 11, and (*b*) area percentage of the remaining monomers (*open symbols*) and the corresponding fragments (*solid symbols*) at 37°C (○ and •) and 50°C (◇ and ◆).

TABLE 1 α-Values in Eq. 12 estimated by fitting the experimental aggregation kinetics data

	Temperature			
Solution type	4°C	25°C	37°C	50°C
0.013 M TFA at pH 2.0	1.0×10^{-5}	6.0×10^{-5}	1.1×10^{-4}	5.0×10^{-4}
0.01 M HCl at pH 2.0		4.6×10^{-5}		
water at pH 4.5		2.7×10^{-6}		

CONCLUSIONS

In this work, we have investigated the dispersion behavior of the RADA 16-I peptide powder in various aqueous solutions. First of all, using several microscopy and LS techniques, we have identified the existence of stable RADA 16-I nanofibrils in the pH range of 2.0–4.5. Such fibrils show a β-sheet structure and have length of around 200–400 nm and diameter of 10 nm. The latter would indicate that each fibril is constituted of two filaments of stretched monomer aligned laterally. These small fibrils cannot be broken by the mechanical stress generated from sonication.

When the peptide powder is dispersed in water at pH 4.5 at a concentration of 1 g/L, all the peptides are in the form of fibrils with an undetectable amount of monomers. When it is dispersed in the 0.013 M TFA or 0.01 M HCl solution at pH 2.0, however, the dispersion contains a substantial amount of monomers. FTIR data indicate that the peptides in the powder are already in the form of fibrils, and the monomers at pH 2.0 arise from dissolution of the fibrils induced by the presence of TFA or Cl.

The stability of the fibril dispersions in water with respect to their incubation time has been investigated at the peptide concentration of 1 g/L. It is found that very slow end-to-end aggregation of the fibrils occurs, leading to elongation of the fibrils without changing their diameter. It has been observed that the monomers do not participate in the fibril elongation. The elongation rate is faster for the peptide dispersion in the presence of TFA or Cl at pH 2.0 than in pure water at pH 4.5, indicating the effect of pH and nature of the anions. The aggregation can be accelerated by temperature in the range of 4–50°C.

The aggregation kinetics under different conditions has been simulated by the Smoluchowski kinetic model, PBE, considering the fibrils to be rod-like. Good agreement between simulations and experiments has been obtained when the incubation time is short, but significant deviation occurs at a long incubation time, where the fibrils most likely grow too long to be considered as rod-like.

It is also found that the aggregation process is not limited by diffusion but rather is an activated process with an energy barrier in the order of 20 kcal/mol.

SUPPORTING MATERIAL

Additional details, six figures, a table, and a reference are available at http://www.biophysj.org/biophysj/supplemental/S0006-3495(12)00322-0.

Financial support from the Swiss National Science Foundation (grant 200020–126487/1) is gratefully acknowledged. The authors thank sincerely Lonza (Visp, Switzerland), in particular Dr. Francesca Quattrini, for supplying material, the Electron Microscopy department of ETH Zurich (EMEZ), in particular Peter Tittmann, Lucas Falk, and Stephan Handschin, for assistance in making cryo-SEM and TEM pictures, and Dr. Xiangyang Zhang (MS service, ETH Zurich) for mass spectrometry analysis.

REFERENCES

1. Zhao, X., and S. Zhang. 2007. Designer self-assembling peptide materials. *Macromol. Biosci.* 7:13–22.
2. Zhang, S., D. M. Marini, …, S. Santoso. 2002. Design of nanostructured biological materials through self-assembly of peptides and proteins. *Curr. Opin. Chem. Biol.* 6:865–871.
3. Yang, Y., U. Khoe, …, S. Zhang. 2009. Designer self-assembling peptide nanomaterials. *Nano Today.* 4:193–210.
4. Aggeli, A., M. Bell, …, N. Boden. 2003. pH as a trigger of peptide β-sheet self-assembly and reversible switching between nematic and isotropic phases. *J. Am. Chem. Soc.* 125:9619–9628.
5. Zhao, X., F. Pan, …, J. R. Lu. 2010. Molecular self-assembly and applications of designer peptide amphiphiles. *Chem. Soc. Rev.* 39:3480–3498.
6. Chen, P. 2005. Self-assembly of ionic-complementary peptides: a physicochemical viewpoint. *Colloids Surf. A Physicochem. Eng. Asp.* 261:3–24.
7. Cavalli, S., F. Albericio, and A. Kros. 2010. Amphiphilic peptides and their cross-disciplinary role as building blocks for nanoscience. *Chem. Soc. Rev.* 39:241–263.
8. D'Auria, G., M. Vacatello, …, L. Paolillo. 2009. Self-assembling properties of ionic-complementary peptides. *J. Pept. Sci.* 15:210–219.
9. Zhang, S., M. A. Greenfield, …, S. I. Stupp. 2010. A self-assembly pathway to aligned monodomain gels. *Nat. Mater.* 9:594–601.
10. Ye, Z., H. Zhang, …, X. Zhao. 2008. Temperature and pH effects on biophysical and morphological properties of self-assembling peptide RADA16-I. *J. Pept. Sci.* 14:152–162.
11. Xiong, H., B. L. Buckwalter, …, M. H. Hecht. 1995. Periodicity of polar and nonpolar amino acids is the major determinant of secondary structure in self-assembling oligomeric peptides. *Proc. Natl. Acad. Sci. USA.* 92:6349–6353.
12. Taraballi, F., M. Campione, …, F. Gelain. 2009. Effect of functionalization on the self-assembling propensity of β-sheet forming peptides. *Soft Matter.* 5:660–668.
13. Marini, D. M., W. Hwang, …, R. D. Kamm. 2002. Left-handed helical ribbon intermediates in the self-assembly of a β-sheet peptide. *Nano Lett.* 2:295–299.
14. Jung, J. P., J. Z. Gasiorowski, and J. H. Collier. 2010. Fibrillar peptide gels in biotechnology and biomedicine. *Biopolymers.* 94:49–59.
15. Zhang, S., T. Holmes, …, A. Rich. 1993. Spontaneous assembly of a self-complementary oligopeptide to form a stable macroscopic membrane. *Proc. Natl. Acad. Sci. USA.* 90:3334–3338.
16. Holmes, T. C., S. de Lacalle, …, S. Zhang. 2000. Extensive neurite outgrowth and active synapse formation on self-assembling peptide scaffolds. *Proc. Natl. Acad. Sci. USA.* 97:6728–6733.
17. Gelain, F., D. Bottai, …, S. Zhang. 2006. Designer self-assembling peptide nanofiber scaffolds for adult mouse neural stem cell 3-dimensional culture. *PLoS One.* 1:e119.
18. Wu, M., Z. H. Yang, …, X. Zhao. 2010. The 3-D culture and in vivo growth of the human hepatocellular carcinoma cell line HepG2 in a self-assembling peptide nanofiber scaffold. *J. Nanomater.* 2010:1–7.
19. Kisiday, J., M. Jin, …, A. J. Grodzinsky. 2002. Self-assembling peptide hydrogel fosters chondrocyte extracellular matrix production and cell division: implications for cartilage tissue repair. *Proc. Natl. Acad. Sci. USA.* 99:9996–10001.
20. Narmoneva, D. A., O. Oni, …, R. T. Lee. 2005. Self-assembling short oligopeptides and the promotion of angiogenesis. *Biomaterials.* 26:4837–4846.
21. Robinson, L. R., N. C. Fitzgerald, …, D. L. Bissett. 2005. Topical palmitoyl pentapeptide provides improvement in photoaged human facial skin. *Int. J. Cosmet. Sci.* 27:155–160.
22. Keller, S., I. Sauer, …, M. Bienert. 2005. Membrane-mimetic nanocarriers formed by a dipalmitoylated cell-penetrating peptide. *Angew. Chem. Int. Ed. Engl.* 44:5252–5255.

23. Fung, S. Y., H. Yang, and P. Chen. 2008. Sequence effect of self-assembling peptides on the complexation and in vitro delivery of the hydrophobic anticancer drug ellipticine. *PLoS One.* 3:e1956.

24. Zhang, S., L. Yan, …, A. Rich. 1999. Biological surface engineering: a simple system for cell pattern formation. *Biomaterials.* 20:1213–1220.

25. Whaley, S. R., D. S. English, …, A. M. Belcher. 2000. Selection of peptides with semiconductor binding specificity for directed nanocrystal assembly. *Nature.* 405:665–668.

26. Hamley, I. W. 2007. Peptide fibrillization. *Angew. Chem. Int. Ed. Engl.* 46:8128–8147.

27. Yokoi, H., T. Kinoshita, and S. Zhang. 2005. Dynamic reassembly of peptide RADA16 nanofiber scaffold. *Proc. Natl. Acad. Sci. USA.* 102:8414–8419.

28. Berne, B., and R. Pecora. 1976. Dynamic Light Scattering. Dover Publications, Mineola, N.Y..

29. Edwards, S. F., and M. Doi. 1986. The Theory of Polymer Dynamics. Oxford University Press, Oxford, UK.

30. Tassieri, M., R. M. L. Evans, …, T. A. Waigh. 2008. The self-assembly, elasticity, and dynamics of cardiac thin filaments. *Biophys. J.* 94:2170–2178.

31. Janmey, P. A., J. Peetermans, …, T. Tanaka. 1986. Structure and mobility of actin filaments as measured by quasielastic light scattering, viscometry, and electron microscopy. *J. Biol. Chem.* 261:8357–8362.

32. Hagenbuchle, M., B. Weyerich, …, R. Weber. 1990. Static light-scattering by aqueous-solutions of rodlike FD-virus particles. *Physica A.* 169:29–41.

33. Lindner, P., and Th. Zemb. 2002. Neutrons, X-rays and Light: Scattering Methods Applied to Soft Condensed Matter. Elsevier Science, Amsterdam, The Netherlands.

34. Sorensen, C. M. 2001. Light scattering by fractal aggregates: a review. *Aerosol Sci. Technol.* 35:648–687.

35. Lattuada, M., P. Sandkühler, …, M. Morbidelli. 2003. Aggregation kinetics of polymer colloids in reaction limited regime: experiments and simulations. *Adv. Colloid Interface Sci.* 103:33–56.

36. Jao, S. C., K. Ma, …, M. G. Zagorski. 1997. Trifluoroacetic acid pretreatment reproducibly disaggregates the amyloid beta-peptide. *Amyloid: Int. J. Exp. Clin. Invest.* 4:240–252.

37. Jun, S., Y. Hong, …, P. Chen. 2004. Self-assembly of the ionic peptide EAK16: the effect of charge distributions on self-assembly. *Biophys. J.* 87:1249–1259.

38. Creighton, T. H. 1993. Proteins: Structures and Molecular Properties. W. H. Freeman, San Francisco.

39. García, M. C. 2005. The effect of the mobile phase additives on sensitivity in the analysis of peptides and proteins by high-performance liquid chromatography-electrospray mass spectrometry. *J. Chromatogr. B Analyt. Technol. Biomed. Life Sci.* 825:111–123.

40. Hill, T. L. 1983. Length dependence of rate constants for end-to-end association and dissociation of equilibrium linear aggregates. *Biophys. J.* 44:285–288.

41. Pallitto, M. M., and R. M. Murphy. 2001. A mathematical model of the kinetics of beta-amyloid fibril growth from the denatured state. *Biophys. J.* 81:1805–1822.

42. Tomski, S. J., and R. M. Murphy. 1992. Kinetics of aggregation of synthetic beta-amyloid peptide. *Arch. Biochem. Biophys.* 294:630–638.